Astronomy & Astrophysics manuscript no. main
November 13, 2025
©ESO 2025

arXiv:2511.09107v1 [astro-ph.IM] 12 Nov 2025

Detection of Lensed Gravitational Waves from dark matter halos with deep learning

Mengfei Sun[1,2], Jie Wu[1,2], Jin Li[1,2,3,⋆], Nan Yang[2,4], Xianghe Ma[1,2], Borui Wang[5], Minghui Zhang[6], and Yuanhong Zhong[7,⋆⋆]

[1] Department of Physics, Chongqing University, Chongqing 401331, P.R. China
[2] Chongqing Key Laboratory for Strongly Coupled Physics, Chongqing University, Chongqing 401331, P.R. China
[3] Institute of Advanced Interdisciplinary Studies, Chongqing University, Chongqing 401331, P.R. China
[4] Department of Electronical Information Science and Technology, Xingtai University, Xingtai 054001, P.R. China
[5] Department of Earth and Space Sciences, Southern University of Science and Technology, Shenzhen 518055, P.R. China
[6] Department of Physics, Southern University of Science and Technology, Shenzhen 518055, P.R. China
[7] School of Microelectronics and Communication Engineering, Chongqing University, Chongqing 401331, P.R. China

November 13, 2025

ABSTRACT

Context. Lensed gravitational waves (GWs) provide a new window into the study of dark matter substructures, yet the faint interference signatures they produce are buried in detector noise.
Aims. To address this challenge, we develop a deep learning framework based on a residual one dimensional convolutional neural network for lensed GW identification under multiband observations.
Methods. The model directly processes multiband waveforms from binary neutron star systems, covering the early inspiral observed by the DECi hertz Interferometer Gravitational wave Observatory (DECIGO) and the late inspiral observed by the Einstein Telescope (ET), which correspond approximately to the wave optics and geometrical optics regimes, respectively. It enables end to end classification of five classes: pure noise, unlensed GWs, and three representative lensed GWs corresponding to singular isothermal sphere (SIS), cored isothermal sphere (CIS), and Navarro–Frenk–White (NFW) profiles. A dataset of 10^6 simulated samples was constructed with signal to noise ratios (SNR) from 5 to 100.
Results. The deep learning model with multiband observations achieves an accuracy of 97.0% and a macro averaged F_1 score of 0.97, significantly exceeding the single detector performance, where DECIGO and ET reach 72.8% and 62.3%, respectively. Even in the low SNR regime (SNR < 20) the model maintains an accuracy above 63%, while in the high SNR regime (SNR > 80) its accuracy approaches 99.8%.
Conclusions. These results demonstrate that multiband GW observations effectively enhance the detection of lensed GWs within complex noise environments, providing a robust and efficient pathway for the automated identification of lensed GWs in future multiband observations.

Key words. lensed gravitational waves – dark matter – deep learning

1. Introduction

With the first direct detection of gravitational waves (GWs) from the binary black hole merger GW150914 (Abbott et al. 2016b) by the LIGO/Virgo Collaboration, GWs astronomy was established as a powerful probe of the Universe under extreme conditions. Since then, numerous events from binary black holes, binary neutron stars, and black hole–neutron star mergers have been observed (Abbott et al. 2017a; DLT40 Collaboration et al. 2017; Abbott et al. 2016a, 2017b, 2021, 2020b,c,a; Collaboration et al. 2021). These detections have verified general relativity in the strong field regime and enabled studies of compact object formation, neutron star equations of state, and cosmological parameters (Schneider 2005; Ehlers & Schneider 2005; Dai & Venumadhav 2017; Kelly et al. 2023; Pascale et al. 2025). Meanwhile, the Λ Cold Dark Matter (ΛCDM) model has become the standard cosmological framework, supported by extensive observations (Alam et al. 2021; Scolnic et al. 2018; Aghanim et al. 2020; Ade et al. 2016; Perlmutter et al. 1999; Riess et al. 1998). Although the ΛCDM paradigm successfully explains large scale structure formation, several small scale discrepancies remain, such as the anomalous X-ray features in galaxy clusters (Bulbul et al. 2014) and the paucity of satellite galaxies in the Milky Way (Koposov et al. 2008). These tensions have motivated alternative dark matter models and efforts to probe dark matter distribution across multiple scales through diverse astronomical observations. Within this context, the lensed GWs has emerged as a new frontier. When a gravitational wave passes near a compact object or dark matter substructure, spacetime curvature modulates its waveform, producing amplitude magnification, phase shifts, and interference fringes (Takahashi & Nakamura 2003; Dai et al. 2018). When the wavelength becomes comparable to the lens's Schwarzschild radius, characteristic wave optics effects arise. These imprints provide unique opportunities to detect low mass dark matter halos and primordial black holes, offering a novel channel for exploring the nature and distribution of dark matter.

⋆ Corresponding author: e-mail: cqujinli1983@cqu.edu.cn
⋆⋆ Corresponding author: e-mail: zhongyh@cqu.edu.cn

Recent theoretical and numerical studies have shown that lensed GWs introduce distinctive amplitude modulations and time delays in the frequency domain, providing a unique probe of dark matter halos and primordial black holes (Tambalo et al. 2023; Leung et al. 2025). Building on these findings, upcoming third generation detectors such as the Einstein Telescope (ET) and the space based DECi hertz Interferometer Gravitational wave Observatory (DECIGO) are expected to enable multiband observations that further enhance the detectability and parameter estimation precision of lensed GWs (Abe et al. 2025; Mukherjee et al. 2020; Li et al. 2023). However, identifying and characterising lensed GWs remain challenging. Traditional matched filtering and Bayesian inference have played a central role in gravitational wave detection and parameter estimation, and continue to provide reliable results across various conditions. As observational sensitivity increases and the volume of detected events grows, these approaches may face practical limitations related to computational efficiency and waveform modeling (Janquart et al. 2021; Li et al. 2018). In particular, low SNR conditions and interference induced modulations can further complicate signal recovery. These developments highlight the importance of exploring complementary and adaptive analysis frameworks for next generation gravitational wave data.

With the rapid development of deep learning and machine learning techniques, these methods have been progressively introduced into gravitational wave data analysis and lensed GWs identification (Kim et al. 2021; Goyal et al. 2021; Li et al. 2025; Liu et al. 2025). Compared with traditional matched filtering and Bayesian inference approaches, deep learning offers advantages in automatic feature extraction and efficient inference. Convolutional neural networks (CNNs) are capable of learning informative representations from time domain or time frequency domain data, which can help mitigate the dependence on predefined waveform templates. Moreover, their inference phase is computationally efficient, making them particularly suitable for real time identification and filtering of the massive number of GWs events expected in future observations (Singh et al. 2018; Goyal et al. 2021). Recent studies have demonstrated the potential of deep learning in identifying lensed GWs (Wilde et al. 2022), further confirming its applicability under various conditions. The advent of third generation detectors has also introduced new opportunities to overcome current limitations through multiband observations. Space based detectors such as the DECIGO exhibits higher sensitivity to low frequency wave optics interference effects, while ground based detectors such as the ET offer superior resolution for geometric optics magnification and phase delay phenomena at mid to high frequencies (Abe et al. 2025). This complementarity across frequency bands implies that, by fusing data from multiple detectors, one can simultaneously exploit multiple scale physical features including diffraction and geometric magnification—to mitigate parameter degeneracies and enhance the accuracy of lensed GWs identification. A deep learning based, multiple detector framework for lensed GWs recognition is therefore expected to play a crucial role in future third generation and space based GWs detectors, providing new methodologies for probing dark matter structures and constraining cosmological parameters.

Building on previous studies, this work proposes a deep learning framework for identifying lensed GWs from binary neutron star (BNS) under multiband observations. The framework uses an improved residual convolutional neural network to perform end to end classification of time domain waveforms in detector noise. Two experimental sets were designed. The first used a unified dataset spanning a signal to noise ratio (SNR) range of 5–100 to train models for single detectors ET, DECIGO, and a multiple detector framework (ET+DECIGO), to investigate the performance improvement achieved through multiband observations. The second divided the data into five SNR intervals to examine performance dependence on SNR. These findings demonstrate that multiband observations significantly enhance the detection and classification of lensed GWs in noisy environments, and highlight their potential for precise automated recognition in future multiband observations.

The paper is structured as follows. Section 1 outlines the scientific motivation and background. Section 2 introduces the theoretical framework of lensed GWs and data generation. Section 3 describes the detector configuration and noise modeling. Section 4 presents the dataset construction and simulation setup. Section 5 details the deep learning architecture and training strategy. Section 6 reports the results and analyses under different detector configurations and SNR. Section 7 concludes with a summary and future outlook.

2. Theoretical Framework

This section outlines the theoretical framework and modelling approach for describing the propagation of GWs through dark matter halo lenses. It introduces the propagation equation under the weak field approximation and summarises the principal characteristics of the adopted mass distribution models.

2.1. Fundamental Theory of Lensed GWs

In the weak field limit, the propagation of GWs through an inhomogeneous spacetime can be described as a perturbation of the background Friedmann–Lemaître–Robertson–Walker (FLRW) metric. Denoting the background metric as $g^B_{\mu\nu}$, the perturbed metric is written as

$$g_{\mu\nu} = g^B_{\mu\nu} + a^2 h_{\mu\nu}, \tag{1}$$

where a is the cosmological scale factor and $h_{\mu\nu}$ is the dimensionless tensor perturbation representing the GWs disturbance. The Newtonian potential of the lens, $\Phi(\mathbf{x})$, satisfies $\Phi \ll 1$ to ensure the validity of the linear approximation. Under this condition, the GWs propagation equation can be approximated as a scalar wave equation with a potential term (Abe et al. 2025):

$$\partial_\mu\left(\sqrt{-g^B}\, g^{\mu\nu}_B\, \partial_\nu h\right) = 0, \tag{2}$$

where $h(\tau, \mathbf{x})$ is the scalar form of the perturbation. Transforming into the frequency domain yields a Helmholtz-like equation (Peters 1974):

$$\left(\nabla^2 + \omega^2\right)\tilde{h} = 4\omega^2\Phi\,\tilde{h}, \tag{3}$$

where $\tilde{h}$ is the frequency domain waveform and $\omega = 2\pi f$ is the angular frequency.

To quantify the lensing modulation, the complex amplification factor is defined (Nakamura & Deguchi 1999; Takahashi & Nakamura 2003):

$$F \equiv \frac{\tilde{h}}{\tilde{h}_{\rm UL}}, \tag{4}$$

where $\tilde{h}_{\rm UL}$ denotes the unlensed waveform. Under the thin lens and Born approximations, F can be expressed as a two dimensional integral over the lens plane (Nakamura & Deguchi 1999;

Takahashi & Nakamura 2003):

$$F(w,y) = \frac{w}{2\pi i}\int d^2x\, \exp[iw\,T(\mathbf{x},\mathbf{y})]\,, \tag{5}$$

where w is the dimensionless frequency parameter proportional to both the observing frequency and the lens mass, y is the dimensionless impact parameter, and $T(\mathbf{x},\mathbf{y})$ is the dimensionless time delay function. Here $\boldsymbol{\xi}$ and $\boldsymbol{\eta}$ denote the two dimensional position vectors on the lens plane and the source plane, respectively. The dimensionless variables are defined as

$$x = \frac{\xi}{\xi_0}, \qquad y = \frac{D_L}{\xi_0 D_S}\eta, \qquad w = \frac{\xi_0^2}{D_{\rm eff}}\omega, \tag{6}$$

where ξ_0 denotes the characteristic length scale of the lens, and $\omega = 2\pi f$ is the angular frequency of the gravitational wave. The effective distance is given by

$$D_{\rm eff} = \frac{D_L D_{LS}}{(1+z_L)D_S}, \tag{7}$$

where D_L, D_S, and D_{LS} are the angular diameter distances from the observer to the lens, from the observer to the source, and from the lens to the source, respectively. The quantity z_L denotes the redshift of the lens. To characterize the lens scale, we define the effective redshifted lens mass as $M_{Lz} = (1+z_L)M_L$, and adopt the normalization $\xi_0 = \sqrt{4GD_{\rm eff}M_{Lz}}$, so that,

$$w = \frac{8\pi G}{c^3}\, M_{Lz}\, f. \tag{8}$$

Hence, w reflects the ratio between the Schwarzschild radius of the lens and the wavelength of the gravitational wave. A large w corresponds to the geometrical optics regime ($w \gg 1$), while a small w corresponds to the wave optics regime ($w \ll 1$) (Abe et al. 2025). In this context, DECIGO mainly operates in the wave optics regime due to its lower frequency, whereas ET approaches the geometrical optics regime at higher frequencies.

The time delay function combines the geometric path difference and the gravitational potential:

$$T(\mathbf{x},\mathbf{y}) = \tfrac{1}{2}|\mathbf{x}-\mathbf{y}|^2 - \psi(\mathbf{x}) - \phi_m(\mathbf{y}), \tag{9}$$

where $\psi(\mathbf{x})$ is the projected lensing potential, and the constant $\phi_m(\mathbf{y})$ normalises the minimum of T to zero. The potential $\psi(\mathbf{x})$ is linked to the surface mass density $\Sigma(\mathbf{x})$ through the two dimensional Poisson equation:

$$\nabla^2_{\mathbf{x}}\psi(\mathbf{x}) = 2\,\frac{\Sigma(\mathbf{x})}{\Sigma_{\rm cr}}, \tag{10}$$

where $\Sigma_{\rm cr} = [4\pi G(1+z_L)D_{\rm eff}]^{-1}$ is the critical surface mass density, and $D_{\rm eff}$ depends on the source lens observer geometry. The theoretical framework above provide the foundation for the subsequent numerical simulations and data analysis.

2.2. Lens Models

To investigate the lensed amplification effects of dark matter halos on GWs, three spherically symmetric mass density models are considered: the Singular Isothermal Sphere, the Cored Isothermal Spher, and the Navarro–Frenk–White profile. These models represent a gradual transition from dense to diffuse halo structures, spanning typical mass distributions from galactic to cluster scales. To focus on the dominant physical effects and maintain analytical tractability, all lenses are assumed to be perfectly spherical, neglecting secondary perturbations and substructure effects (Poon et al. 2025). The analysis is performed under the thin lens and weak field approximations, allowing the amplification factor $F(f,y)$ to be derived in a unified formalism.

Singular Isothermal Sphere (SIS) The SIS model describes self-gravitating systems with constant velocity dispersion. Its three dimensional density is

$$\rho(r) = \frac{v^2}{2\pi G r^2}, \tag{11}$$

where v is the velocity dispersion. The corresponding surface density is

$$\Sigma(x) = \frac{v^2}{2G\xi_0 x}. \tag{12}$$

When $v^2 = G\Sigma_{\rm cr}\xi_0$, the scale ξ_0 equals the Einstein radius, giving $\kappa(x) = 1/(2x)$ and lensing potential

$$\psi(x) = x. \tag{13}$$

The frequency domain amplification factor is expressed analytically as a hypergeometric series (Matsunaga & Yamamoto 2006):

$$F(w,y) = e^{iwy^2/2}\sum_{n=0}^{\infty}\frac{\Gamma(1+n/2)}{n!}\left(2we^{i3\pi/2}\right)^{n/2} \times {}_1F_1\left(1+\frac{n}{2};\,1;\,-\frac{iwy^2}{2}\right), \tag{14}$$

where w is the dimensionless frequency parameter. As y decreases, interference fringes become sharper and magnification stronger.

Cored Isothermal Sphere (CIS) The CIS model extends the SIS profile by introducing a finite core radius r_c, representing halos with flattened central densities (Kormann et al. 1994; Flores & Primack 1996; Treu 2010). Its three dimensional and surface densities are

$$\rho(r) = \rho_0\,\frac{r_c^2}{r^2+r_c^2}, \qquad \Sigma(x) = \frac{\pi\rho_0 x_c\xi_0}{\sqrt{(x/x_c)^2+1}}, \tag{15}$$

where $x_c = r_c/\xi_0$. For $\rho_0 = \Sigma_{\rm cr}/(2\pi\xi_0 x_c^2)$, ξ_0 corresponds to the Einstein radius. The lensing potential is

$$\psi(x) = \sqrt{x^2+x_c^2} + x_c\ln\left(\frac{2x_c}{\sqrt{x^2+x_c^2}+x_c}\right). \tag{16}$$

Compared with the SIS model, the CIS profile yields a smoother central potential. Increasing x_c weakens focusing and reduces fringe contrast. The amplification factor must be obtained numerically, depending on (w,y,x_c).

Navarro–Frenk–White (NFW) The NFW profile, derived from cosmological N body simulations, describes cold dark matter halos (Navarro 1996; Navarro et al. 1997):

$$\rho(r) = \frac{\rho_s}{(r/r_s)(1+r/r_s)^2}. \tag{17}$$

Defining $x_s = r_s/\xi_0$, the surface density is

$$\Sigma(x) = 2\rho_s r_s\,\frac{1-g(x/x_s)}{(x/x_s)^2-1}, \tag{18}$$

where

$$g(a) = \begin{cases} \dfrac{\arctan\sqrt{a^2-1}}{\sqrt{a^2-1}}, & a > 1, \\ \dfrac{\operatorname{arctanh}\sqrt{1-a^2}}{\sqrt{1-a^2}}, & a < 1, \\ 1, & a = 1. \end{cases} \tag{19}$$

For $\rho_s = \Sigma_{\rm cr}/(4x_s^3\xi_0)$, the lensing potential becomes

$$\psi(x) = \tfrac{1}{2}\left[\ln^2\left(\frac{x}{2x_s}\right) + ((x/x_s)^2 - 1)g^2(x/x_s)\right]. \tag{20}$$

The frequency domain properties of the NFW model are sensitive to r_s: smaller r_s yields more concentrated halos, stronger magnification, denser fringes, and higher modulation contrast.

In this work, the amplification factors $F(w, y)$ for the three representative dark matter halo lens models (SIS, CIS, and NFW)were computed using the `GLoW_public` library (Villarrubia-Rojo et al. 2025).

3. Detector Configuration and Noise Modeling

This section outlines the detector configurations and noise models adopted in this study. It first introduces the representative detector systems and their sensitivity characteristics, followed by discussions of the antenna response functions (Sec. 3.2) and the modelling of detector noise (Sec. 3.3). A unified specification of these components ensures geometric and noise consistency between the DECIGO and the ET, establishing a consistent basis for waveform simulation and signal analysis of lensed GWs.

3.1. Detector Systems and Sensitivity Characteristics

This study considers two representative next generation GWs detectors: the space based DECIGO (Yagi & Seto 2011; Kawamura et al. 2021; Tsuji et al. 2024) and the ground based ET (Regimbau et al. 2012; Punturo et al. 2010; Hild et al. 2009). These instruments are complementary in sensitivity and operational frequency range, covering approximately 0.1-10 Hz for DECIGO and 10-1000 Hz for ET. The inspiral phase of BNS merger spans frequencies from 0.1 to 10^3 Hz, tracing the system's evolution from early orbital contraction to the pre-merger stage. DECIGO is thus sensitive to the low frequency early inspiral, whereas ET captures the mid to high frequency band preceding coalescence. The noise power spectral density (PSD) for DECIGO follows the official design specification (Yagi & Seto 2011), and that for ET is based on the ET sensitivity curve (Hild et al. 2011).

Fig. 1 compares the PSD of DECIGO and ET with the amplitude spectral density (ASD) of a typical BNS signal. DECIGO achieves higher sensitivity in the 0.1-10 Hz band, enabling the detection of interference and diffraction features produced by low mass lenses dominated by wave optics effects. In contrast, ET exhibits superior response in the 20-200 Hz range, where geometric optics amplification and phase shifts prevail. The complementarity of their frequency coverage allows the same merger event to be jointly observed during different inspiral stages, yielding a more complete waveform and enhancing the accuracy of lens type classification.

3.2. Detector Response Functions

In multiband observations, the detector response functions describe how the detected strain couples to the source direction, polarization, and detector orientation. For an arbitrary GW source,

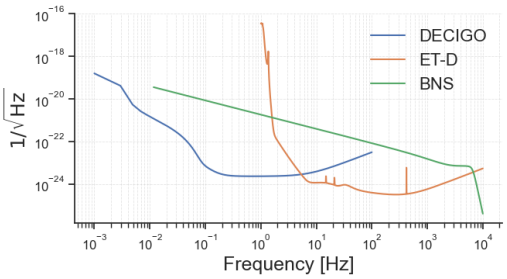

Fig. 1: Amplitude spectral densitie (ASD) of DECIGO and ET compared with that of a representative BNS gravitational wave.

the measured strain at the detector is expressed as

$$h_{\rm det}(t) = F_+(t)\,h_+(t) + F_\times(t)\,h_\times(t), \tag{21}$$

where F_+ and $F_\times$ are the antenna pattern functions for the "+" and "×" polarization modes, respectively, and h_+ and $h_\times$ denote the corresponding waveform components. These response functions encode the time dependent coupling between the incident direction (θ, ϕ), the polarization angle ψ, and the detector geometry.

DECIGO is a space based interferometer with a triangular three arm configuration whose antenna response varies periodically with time. Let $(\bar\theta_S, \bar\phi_S)$ denote the source position in the heliocentric coordinate system and $(\hat\theta_L, \hat\phi_L)$ the orientation of the orbital angular momentum. The observed strain in the detector frame is (Yagi & Seto 2011)

$$h(t) = F_+(\bar\theta_S, \bar\phi_S, \hat\theta_L, \hat\phi_L)\,h_+(t) + F_\times(\bar\theta_S, \bar\phi_S, \hat\theta_L, \hat\phi_L)\,h_\times(t), \tag{22}$$

where

$$F_+(\theta_S, \phi_S, \psi_S) = \frac{1}{2}\left(1 + \cos^2\theta_S\right)\cos(2\phi_S)\cos(2\psi_S) - \cos\theta_S\,\sin(2\phi_S)\sin(2\psi_S), \tag{23}$$

$$F_\times(\theta_S, \phi_S, \psi_S) = \frac{1}{2}\left(1 + \cos^2\theta_S\right)\cos(2\phi_S)\sin(2\psi_S) + \cos\theta_S\,\sin(2\phi_S)\cos(2\psi_S). \tag{24}$$

The transformation between the angular parameters $(\theta_S, \phi_S, \psi_S)$ and the heliocentric coordinates is given by

$$\theta_S(t) = \cos^{-1}\left[\frac{1}{2}\cos\bar\theta_S - \frac{\sqrt{3}}{2}\sin\bar\theta_S\cos(\hat\phi(t) - \bar\phi_S)\right], \tag{25}$$

$$\phi_S(t) = \frac{\pi}{12} + \tan^{-1}\left[\frac{\sqrt{3}\cos\bar\theta_S + \sin\bar\theta_S\cos(\hat\phi(t) - \bar\phi_S)}{2\sin\bar\theta_S\sin(\hat\phi(t) - \bar\phi_S)}\right], \tag{26}$$

$$\psi_S = \tan^{-1}\left(\frac{a}{b}\right), \tag{27}$$

where

$$a = \frac{1}{2}\cos\hat{\theta}_L - \frac{\sqrt{3}}{2}\sin\hat{\theta}_L\cos[\hat{\phi}(t) - \hat{\phi}_L] - \cos\hat{\theta}_L\cos^2\bar{\theta}_S - \sin\hat{\theta}_L\sin\bar{\theta}_S\cos(\hat{\phi}_L - \bar{\phi}_S), \quad (28)$$

$$b = \frac{1}{2}\sin\hat{\theta}_L\sin\bar{\theta}_S\sin(\hat{\phi}_L - \bar{\phi}_S) - \frac{\sqrt{3}}{2}\cos\hat{\phi}(t)[\cos\hat{\theta}_L\sin\bar{\theta}_S\sin\bar{\phi}_S - \cos\bar{\theta}_S\sin\hat{\theta}_L\sin\hat{\phi}_L] - \frac{\sqrt{3}}{2}\sin\hat{\phi}(t)[\cos\bar{\theta}_S\sin\hat{\theta}_L\cos\hat{\phi}_L - \cos\hat{\theta}_L\sin\bar{\theta}_S\cos\bar{\phi}_S], \quad (29)$$

and

$$\bar{\theta}(t) = \pi/2, \qquad \hat{\phi}(t) = 2\pi t/T + c_0, \quad (30)$$

where $T = 1$ yr is the orbital period and $c_0 = 0$ is the initial orbital phase.

The Einstein Telescope consists of three co-located interferometers arranged in an equilateral triangle, each having equal arm lengths and an opening angle of $\gamma = \pi/3$. Let (θ, ϕ) denote the source sky location in the detector frame and ψ the polarization angle. For a single interferometer with arm orientation offset Δ, the antenna pattern functions for the plus and cross polarizations are given by (Hild et al. 2011)

$$F_+(\theta,\phi,\psi;\gamma,\Delta) = -\frac{\sin\gamma}{2}\Big[(1+\cos^2\theta)\sin(2\phi')\cos(2\psi) + 2\cos\theta\cos(2\phi')\sin(2\psi)\Big], \quad (31)$$

$$F_\times(\theta,\phi,\psi;\gamma,\Delta) = +\frac{\sin\gamma}{2}\Big[(1+\cos^2\theta)\sin(2\phi')\sin(2\psi) - 2\cos\theta\cos(2\phi')\cos(2\psi)\Big], \quad (32)$$

where $\phi' = \phi + \Delta$. In the ET-D configuration, the three interferometers are oriented with relative rotation angles $\Delta = 0, +2\pi/3$, and $-2\pi/3$, corresponding to three 60° separated arms forming an equilateral triangle layout underground. Each interferometer therefore provides an independent response following the same functional form but rotated in azimuth by Δ.

For data generation, the directional response is averaged over random sky positions and polarization angles, approximating an isotropic source distribution. To ensure geometric consistency between DECIGO and ET for the same GW source, a reference epoch $t_{\rm ref}$ in the heliocentric coordinate system is defined, and the polarization angle ψ is fixed accordingly using the DECIGO transformation (equations (28)–(29)) with $t = t_{\rm ref}$:

$$\bar{\phi}_t = \frac{2\pi}{T}t_{\rm ref} + c_0, \qquad \psi = \tan^{-1}\left(\frac{a}{b}\right), \quad (33)$$

In the ET response, the parameters are then set to

$$\theta = \bar{\theta}_S, \qquad \phi = \bar{\phi}_S, \qquad \psi = \psi(t_{\rm ref}), \quad (34)$$

where $(\bar{\theta}_S, \bar{\phi}_S)$ are the source sky coordinates, and $\psi(t_{\rm ref})$ is the polarization angle determined by the DECIGO geometry at the reference epoch. Here the reference time is set to $t_{\rm ref} = 0$, corresponding to the initial orbital phase of DECIGO. This configuration guarantees that both detectors share identical source direction and polarization orientation when observing the same GW event, ensuring full geometric consistency.

3.3. Noise Modeling and Detector Noise Generation

Based on the one sided noise PSD, we could obtain the time domain noise signal from the one sided PSD; in this paper, we utilized the Python function `pycbc.noise.gaussian.noise_from_psd` (Nitz et al. 2024), which takes a PSD as input and returns colored Gaussian noise, to simulate the time domain noise received by both the DECIGO and ET detectors. The corresponding PSDs of ET and DECIGO were adopted according to their official sensitivity curves (Yagi & Seto 2011; Hild et al. 2011), ensuring that the generated noise realizations accurately reflect the instrumental characteristics across their respective frequency bands.

4. Dataset Construction and Simulation Setup

Under the thin lens and weak field approximations, the lensed GWs can be modelled as a frequency domain modulation of the unlensed (UL) signal. The UL polarization components $\tilde{h}_+^{\rm UL}(f)$ and $\tilde{h}_\times^{\rm UL}(f)$ are first generated, and the corresponding lensed signals are obtained by multiplying them by the amplification factor $F(w, y)$:

$$\tilde{h}_+(f) = F(w,y)\,\tilde{h}_+^{\rm UL}(f), \qquad \tilde{h}_\times(f) = F(w,y)\,\tilde{h}_\times^{\rm UL}(f), \quad (35)$$

where $\tilde{h}_+(f)$ and $\tilde{h}_\times(f)$ denote the "+" and "×" polarization components after lensing modulation, and $\tilde{h}_+^{\rm UL}(f)$ and $\tilde{h}_\times^{\rm UL}(f)$ are their unlensed counterparts. The amplification factor $F(w, y)$ depends on the adopted lens model and includes three classes in this study:

$$F(w,y) \in \{F_{\rm SIS}(w,y),\ F_{\rm CIS}(w,y),\ F_{\rm NFW}(w,y)\}, \quad (36)$$

corresponding to the SIS, CIS, and NFW dark matter halo models.

Applying an inverse Fourier transform to the modulated frequency domain signals yields the time domain polarization waveforms $h_+(t)$ and $h_\times(t)$. Considering the detector antenna responses, the measured strain is given by

$$h(t) = F_+(t;\Omega,\psi)\,h_+(t) + F_\times(t;\Omega,\psi)\,h_\times(t), \quad (37)$$

where F_+ and $F_\times$ are the response functions to the two polarizations, Ω denotes the sky location of the source, and ψ is the polarization angle. Finally, detector noise $n(t)$ consistent with the detector PSD $S_n(f)$ is added to obtain the simulated observation:

$$s(t) = h(t) + n(t), \quad (38)$$

where $s(t)$ is the final noisy observation and $n(t)$ is a Gaussian noise sequence with spectral structure defined by $S_n(f)$. This procedure comprises four stages, including lensing modulation, Fourier transformation, detector response mapping, and noise injection.

For both the space based DECIGO and the ground based ET detectors, five classes of samples were generated: pure noise (PN), unlensed (UL), and three lensed cases (SIS, CIS, NFW). The physical parameters of the BNS, including component masses and luminosity distances, were randomly and uniformly sampled according to Table 1. To evaluate the impact of SNR on classification performance, the data were stratified by the SNR of the UL signal in noise, divided into five intervals: 5-20, 20-40, 40-60, 60-80, and 80-100. Each SNR interval contained an independent dataset comprising five signal classes (PN, UL, SIS, CIS, NFW) with 4×10^4 samples per class, yielding 2×10^5 samples per set. All signals shared the same parameter sampling scheme but differed in noise realizations, lens

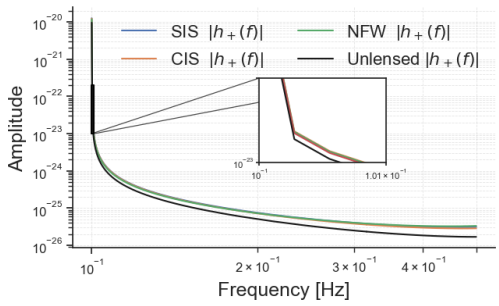

(a) Frequency domain waveforms of DECIGO.

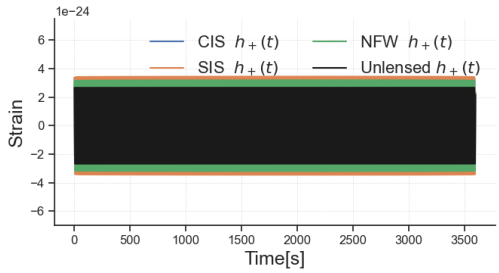

(b) Time domain waveforms of DECIGO.

Fig. 2: Frequency and time domain waveforms of BNS ($m_1 = m_2 = 1.4\,M_\odot$, $d_L = 100$ Mpc) under SIS, CIS, and NFW lensing models, as observed by DECIGO. The lens parameters are $M_L = 2\times10^3\,M_\odot$, $\psi_0 = 1.0$, $r_c = 0.3$, $r_s = 0.3$, and $y = 0.3$.

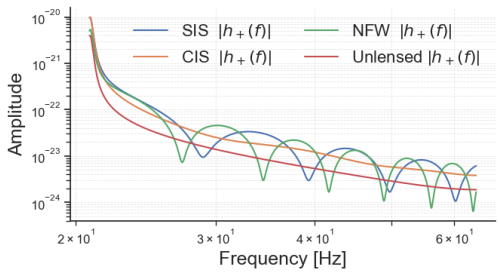

(a) Frequency domain waveforms of ET.

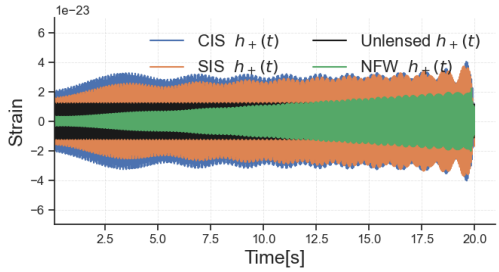

(b) Time domain waveforms of ET.

Fig. 3: Frequency and time domain waveforms of ($m_1 = m_2 = 1.4\,M_\odot$, $d_L = 100$ Mpc) under SIS, CIS, and NFW lensing models, as observed by ET. The lens parameters are $M_L = 2\times10^3\,M_\odot$, $\psi_0 = 1.0$, $r_c = 0.3$, $r_s = 0.3$, and $y = 0.3$.

classes, and modulation parameters. For each detector, datasets were generated following identical SNR intervals and sample counts, ensuring direct comparability between DECIGO and ET under matched physical conditions. The definitions of all sample classes are listed in Table 2.

Table 1: Sampling ranges of BNS waveform parameters. The source parameters were fixed at inclination $\iota = 1.0$, initial phase $\phi_0 = 0$, and dimensionless spins $\chi_1 = \chi_2 = 0.1$. The angular parameters $(\bar{\theta}_S, \bar{\phi}_S, t_{\rm ref})$ correspond to the DECIGO response geometry, where the polarization angle ψ is computed at the fixed reference epoch $t_{\rm ref} = 0$ according to Eq. (33). For the ET response, the parameters are determined as $(\theta, \phi, \psi)_{\rm ET} = (\bar{\theta}_S, \bar{\phi}_S, \psi)$ to ensure geometric consistency with DECIGO.

Parameter	Symbol	Range
Primary mass	m_1	$\mathcal{U}(1,3)\,M_\odot$
Secondary mass	m_2	$\mathcal{U}(1,3)\,M_\odot$
Luminosity distance	D_L	$\mathcal{U}(0,10^3)$ Mpc
Ecliptic latitude	$\bar{\theta}_S$	$\cos^{-1}(\mathcal{U}(-1,1))$
Ecliptic longitude	$\bar{\phi}_S$	$\mathcal{U}(0,2\pi)$
Reference epoch	$t_{\rm ref}$	0 (fixed)

After generating the SNR stratified datasets, the data were further organized for different experimental configurations. For each detector (ET or DECIGO), all SNR intervals were merged into a unified full range dataset spanning 5-100, comprising roughly 10^6 samples, to train single detector models and evaluate overall classification performance. To enable a fair comparison with models trained on individual detectors, a model was trained on the combined dataset from the multiple detector configuration (ET+DECIGO), within the same SNR range. This approach allows us to evaluate the potential performance gains introduced by multiband observations. Additionally, to investigate the effect of SNR, we trained and evaluated separate models across five distinct SNR intervals.

DECIGO operates within the 0.1-10 Hz band, with a sampling rate of 1 Hz and signal duration of 3600 s, while ET covers 20-200 Hz with a sampling rate of 128 Hz and duration of 20 s. The waveform templates were generated based on the post-Newtonian model described in Ref. Wu et al. (2024); Blanchet (2024, 2019); Cho et al. (2022), adopting a 2.5PN approximation including spin–orbit (SO) coupling while neglecting spin–spin (SS) effects. The BNS component masses and luminosity distance were sampled according to Table 2, while the remaining source parameters were fixed at inclination $\iota = 1.0$, initial phase $\phi_0 = 0$, and dimensionless spins $\chi_1 = \chi_2 = 0.1$. The amplification factor $F(w, y)$ was computed numerically using the `GLoW_public` (Villarrubia-Rojo et al. 2025), with fixed lens parameters $M_L = 2\times10^3\,M_\odot$, $y = 0.3$, $x_c = 0.3$, and $x_s = 0.3$, where M_L is the lens mass, y is the dimensionless impact parameter, and x_c and x_s are the dimensionless core radii for the CIS and NFW models, respectively.

For the adopted parameters, the characteristic time delay between multiple images can be estimated as(Abe et al. 2025)

$$\Delta t_{\rm d} \simeq 0.03\left(\frac{M_{Lz}}{3\times10^3 M_\odot}\right)\left(\frac{y}{0.3}\right)\ {\rm s}. \tag{39}$$

We found that in the ET frequency band, the inspiral waveform of the BNS system yields a time delay close to zero under these conditions. Therefore, in the subsequent analysis, the interference between multiple images was neglected. Representative frequency and time domain waveforms generated under these settings are illustrated in Fig. 2 and Fig. 3, corresponding to a binary neutron star system with the same lens parameters.

Detector noise was generated based on the PSD specific to each detector. After applying lensing modulation, detector response, and noise addition, the time domain signals for each detector were individually adjusted in length. Longer waveforms

Table 2: frequency domain construction and time domain forms of the five sample classes (each $\sim 10^5$ samples). Here, $\tilde{h}^{\rm UL}(f)$ denotes the UL frequency domain waveform, $F(w)$ is the frequency domain amplification factor, $h(t)$ is the detector response convolved strain, and $n(t)$ is detector noise.

Class	frequency domain form	time domain form
PN	-	$n(t)$
UL	$\tilde{h}^{\rm UL}(f)$	$h(t) + n(t)$
SIS	$F_{\rm SIS}(w, y)\,\tilde{h}^{\rm UL}(f)$	$h^{\rm SIS}(t) + n(t)$
CIS	$F_{\rm CIS}(w, y)\,\tilde{h}^{\rm UL}(f)$	$h^{\rm CIS}(t) + n(t)$
NFW	$F_{\rm NFW}(w, y)\,\tilde{h}^{\rm UL}(f)$	$h^{\rm NFW}(t) + n(t)$

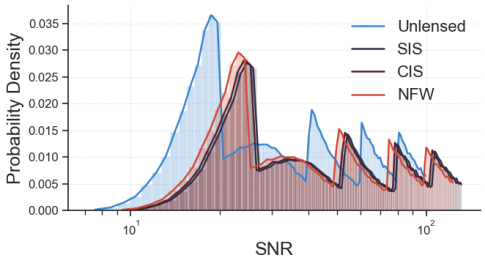

(a) SNR distribution for DECIGO.

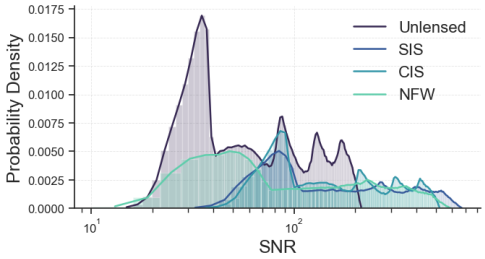

(b) SNR distribution for ET.

Fig. 4: SNR distributions of simulated samples for DECIGO and ET detectors.

were truncated, while shorter ones were padded with zeros. This ensured consistent alignment in time within each detector's dataset. The resulting dataset includes standardized waveforms across five classes, multiple SNR intervals, and both single and multiple detector configurations. Figure 4 shows the SNR distributions of all sample classes in the constructed dataset. DECIGO and ET exhibit complementary sensitivities: DECIGO is more responsive to low frequency, interference dominated features, whereas ET is more sensitive in the mid to high frequency regime dominated by geometric amplification.

5. Deep Learning Architecture and Training Strategy

To enable efficient and robust classification of dark matter halo lensing effects, we developed a residual stacked one dimensional convolutional neural network (ResNet-like 1D CNN) that operates directly on time domain waveform inputs. The model classifies five classes: PN, UL signals, and three lensed cases corresponding to the SIS, CIS, and NFW models. By processing standardized time domain strain sequences without frequency domain transformation or handcrafted feature extraction, the network retains temporal continuity and local interference structures, which are expected to contribute to better recognition of weak modulations.

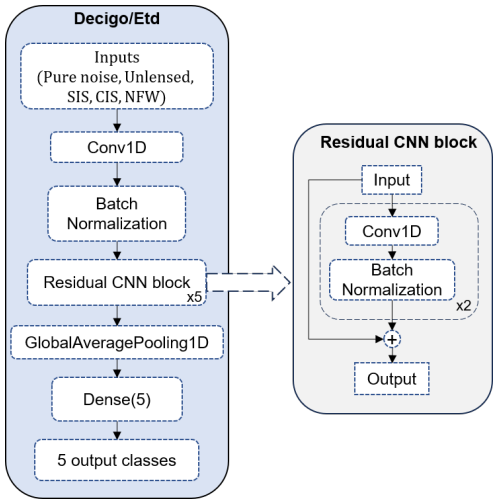

Fig. 5: Architecture of the residual stacked convolutional network.

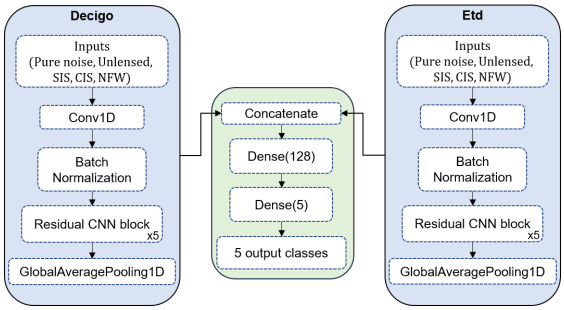

Fig. 6: A dual branch network that combines features from two detectors (ET and DECIGO) using late fusion.

The architecture comprises multiple residual convolutional modules, each containing two convolution–normalization–activation (ReLU) layers with identity shortcuts to facilitate feature propagation and alleviate vanishing gradient or degradation effects. The input first passes through an initial 1D convolutional layer for primary feature extraction, followed by five stacked residual blocks forming deep hierarchical channels. Each block applies a 3×1 convolution kernel, Batch Normalization, and a ReLU activation. A global average pooling layer compresses the temporal dimension, and a fully connected layer with a Softmax activation outputs the five class probability distribution. The complete single branch network functions as an end to end multiple class classifier (Fig. 5).

To evaluate the benefit of multiband observations, two network configurations were implemented. The first is a single branch network processing input waveforms from either DECIGO or ET individually. The second is a dual branch fusion network designed for multiple detector inputs, where each branch independently processes data from one detector using identical ResNet substructures. Deep feature maps from both branches are concatenated in feature space and fused via a fully connected layer to form a unified representation. This late fusion approach preserves detector specific feature learning while leveraging the complementarity between the low frequency (DECIGO) and mid to high frequency (ET) bands, thereby enhancing discrimination of both interference-diffraction patterns and geometric magnification effects (Fig. 6).

All input waveforms were standardized to zero mean and unit variance to improve numerical stability and convergence. The model was optimized using sparse categorical cross entropy loss and the Adam optimizer with an initial learning rate of 10^{-3}. The `ReduceLROnPlateau` strategy was employed to decrease the learning rate adaptively when the validation loss stagnated, and `EarlyStopping` was used to terminate training when no improvement was observed for several epochs. Training was performed for up to 200 epochs with a batch size of 128 and a 10% validation split. All experiments used fixed length waveform sequences and five classes output labels. Model training and inference were accelerated using an NVIDIA A800 80G GPU and two Intel(R) Xeon(R) Silver 8480 CPU.

6. Results and Analysis

This section evaluates the model's classification performance under different detector setups and SNR conditions. The analysis is divided into two parts. First, using datasets that span the full SNR range of unlensed signals (0-100), we evaluate and compare the classification results of models trained on individual detectors (ET and DECIGO) with those trained on combined data from both detectors. This comparison helps to quantify the effect of using multiple detectors on overall performance. Second, we examine how classification accuracy varies with SNR within the multiple detector configuration, to better understand how signal strength influences detection sensitivity and the reliability of lens classification.

6.1. Single and Multiple Detector Performance

Using a comprehensive dataset spanning the 0-100 SNR range, we evaluated the model's classification performance across five classes: PN, UL signals, and three representative lensing models (SIS, CIS, and NFW). Three input configurations were tested: single detector ET, single detector DECIGO, and the multiple detectors (ET+DECIGO). The dataset was divided into training and testing subsets in a 9:1 ratio. Each class contained 4×10^4 samples, corresponding to 3.6×10^4 training and 4×10^3 testing samples per class, giving a total of 1.8×10^5 training and 2×10^4 testing samples.

Model performance was evaluated using Accuracy, Precision, Recall, F_1 score, and Macro Average metrics. Accuracy quantifies the overall classification correctness and is defined as

$$\text{Accuracy} = \frac{TP + TN}{TP + TN + FP + FN}, \tag{40}$$

where TP, TN, FP, and FN denote true positives, true negatives, false positives, and false negatives, respectively. Although the above definition corresponds to binary classification, the accuracy reported in this study represents the overall mean value computed across all five lensing classes, providing a single metric that summarizes the model's global classification performance. Precision and Recall measure the reliability and completeness of the predictions:

$$\text{Precision} = \frac{TP}{TP + FP}, \qquad \text{Recall} = \frac{TP}{TP + FN}. \tag{41}$$

The F_1 score provides a harmonic mean of Precision and Recall:

$$F_1 = \frac{2\,\text{Precision} \times \text{Recall}}{\text{Precision} + \text{Recall}}. \tag{42}$$

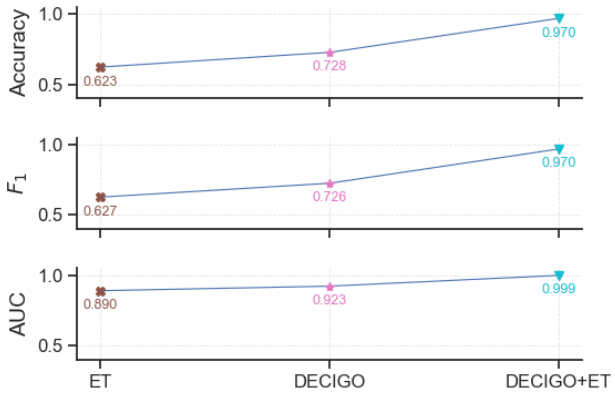

Fig. 7: The classification Accuracy, average F_1, and average AUC for ET, DECIGO, and joint (ET+DECIGO) models.

Table 3: Classification performance metrics for the ET model.

Class	Precision	Recall	F_1 score
PN	0.7528	0.7275	0.7400
UL	0.4347	0.7205	0.5423
SIS	0.6437	0.5999	0.6210
CIS	0.7147	0.6178	0.6627
NFW	0.7752	0.4494	0.5689
Macro average	0.6642	0.6230	0.6270
Accuracy		0.6230	

For multiple class classification, Macro Averaging is applied to balance contributions among all C classes:

$$\text{Micro average}(M) = \frac{1}{C}\sum_{i=1}^{C} M_i, \tag{43}$$

where M_i is the metric for class i.

To further analyse inter class discrimination, confusion matrices were plotted to visualise misclassification relationships among classes, and Receiver Operating Characteristic (ROC) curves were constructed to evaluate the trade off between the True Positive Rate (TPR) and False Positive Rate (FPR). The Area Under the Curve (AUC) quantifies the model's discriminative ability:

$$\text{AUC} = \int_0^1 \text{TPR}(\text{FPR})\, d(\text{FPR}), \tag{44}$$

where larger AUC values (approaching 1) indicate stronger separation capability.

Comprehensive comparisons under different input configurations are summarised in Tables 3-5. The accuracy, average F_1, and average AUC trends are shown in Fig. 7, and the corresponding ROC curves and confusion matrices are presented in Fig. 8 and Fig. 9, respectively.

The ET model demonstrates limited classification capability in the mid to high frequency regime, achieving an accuracy of 0.623 and a macro averaged F_1 score of 0.627. This indicates that high frequency information alone is insufficient to capture the wave optics features of lensed GWs signals. For the "PN" and "UL" classes, the Precision and Recall values are 0.75/0.73 and 0.43/0.72, respectively, revealing substantial false negatives and misclassifications under low SNR conditions. Among the lensed classes, the model's recognition remains limited, with

Table 4: Classification performance metrics for the DECIGO model.

Class	Precision	Recall	F_1 score
PN	0.9993	1.0000	0.9996
UL	0.9294	0.9945	0.9609
SIS	0.5183	0.5626	0.5396
CIS	0.9301	0.4149	0.5738
NFW	0.4766	0.6636	0.5548
Macro average	0.7707	0.7271	0.7257
Accuracy		0.7280	

Table 5: Classification performance metrics for the joint (ET+DECIGO) model.

Class	Precision	Recall	F_1 score
PN	1.0000	1.0000	1.0000
UL	0.9960	0.9998	0.9979
SIS	0.9441	0.9068	0.9251
CIS	0.9146	0.9987	0.9548
NFW	1.0000	0.9444	0.9714
Macro average	0.9709	0.9699	0.9698
Accuracy		0.9700	

$F_{1,\mathrm{SIS}} = 0.621$, $F_{1,\mathrm{CIS}} = 0.663$, and $F_{1,\mathrm{NFW}} = 0.569$. In particular, the NFW class exhibits a Recall of only 0.449, reflecting poor sensitivity to weak interference structures. The generally low F_1 scores suggest that the model struggles to maintain a balance between precision and recall, implying incomplete extraction of lensing related features.

The confusion matrix (Fig. 9a) further reveals notable confusion between the SIS and CIS classes, with roughly 22% of samples misclassified, and several NFW signals incorrectly labelled as UL or PN. The ROC curve (Fig. 8) shows that the ET model's TPR remains low in the small FPR region, indicating weak detection performance under strict classification thresholds. This degradation arises primarily because the network fails to capture low frequency phase interference patterns, leading the decision boundaries to depend largely on amplitude variations. As a result, feature separability is reduced, producing unstable classification outcomes. Nevertheless, the ET model retains moderate sensitivity to strong geometric amplification signatures from high mass lenses, providing complementary information for subsequent multiband fusion analysis.

The DECIGO model, leveraging low frequency diffraction and phase interference information, achieves a notable improvement in overall performance. Its accuracy reaches 0.728, with a macro averaged F_1 score of 0.726, demonstrating enhanced sensitivity to interference structures in the low frequency band. For the "PN" and "UL" classes, the F_1 scores reach 0.9996 and 0.961, respectively, indicating near perfect recognition. However, for the three lensing cases (SIS, CIS, and NFW), the F_1 scores are 0.540, 0.574, and 0.555, respectively, revealing residual confusion. The confusion matrix (Fig. 9b) shows that misclassification between SIS and CIS occurs at a rate of approximately 25–30%, while around 72% of NFW signals are incorrectly labelled as other lens classes.

ROC analysis (Fig. 8) indicates that DECIGO maintains a high TPR even at low FPR, with an average AUC of about 0.90, substantially outperforming ET. This result confirms that low frequency data enhances both phase sensitivity and noise robustness. Overall, DECIGO achieves superior classification stability in weak signal regimes compared with ET, demonstrating the advantage of low frequency interference patterns under complex noise conditions.

Table 6: Classification metrics of the joint (ET+DECIGO) model in the SNR range 5–20.

Class	Precision	Recall	F_1 score
PN	1.0000	1.0000	1.0000
UL	0.7791	0.8316	0.8045
SIS	0.5114	0.3910	0.4431
CIS	0.5662	0.1460	0.2321
NFW	0.4214	0.7901	0.5496
Macro average	0.6556	0.6317	0.6059
Accuracy		0.6339	

The joint model (ET+DECIGO) demonstrates a substantial performance gain through multiband fusion. It achieves an accuracy of 0.970, with macro averaged Precision, Recall, and F_1 values of 0.971, 0.970, and 0.970, respectively (Table 5), clearly surpassing both single detector models. For the "PN" and "UL" classes, F_1 scores reach 1.000 and 0.998, indicating near perfect recognition. The three lensed classes also show significant improvement, with $F_{1,\mathrm{SIS}} = 0.925$, $F_{1,\mathrm{CIS}} = 0.955$, and $F_{1,\mathrm{NFW}} = 0.971$.

The confusion matrix (Fig. 9c) exhibits strong diagonal dominance, with mutual misclassification between SIS and CIS below 2%, and NFW misclassification below 1%. The ROC curves (Fig. 8) show that the joint model completely encompasses both single detector models, with a micro average AUC approaching unity and individual class AUCs improving by about 0.10-0.25. This demonstrates a clear enhancement in both sensitivity and stability.

The accuracy trend (Fig. 7) further confirms the monotonic improvement from ET (62.3%) to DECIGO (72.8%) to the joint model (97.0%). The superiority of the joint configuration arises from multiband feature complementarity: the low frequency channel contributes phase interference information, while the high frequency channel captures amplitude and propagation delay signatures. Their combination enhances the model's discriminative capability and noise robustness.

Overall, based on the metrics in Tables 3-5 and the visual comparisons in Figs. 8-9, the ET+DECIGO joint model outperforms both single detector counterparts in accuracy, confusion structure, and robustness, confirming the physical and statistical advantages of multiband data fusion for detecting lensed GWs in noisy environments.

6.2. Performance of the Multiple Detector at Different SNR

To evaluate the robustness and sensitivity of the multiple detector (ET+DECIGO) model under varying SNR, the model was trained and evaluated separately within five SNR intervals: 5-20, 20-40, 40-60, 60-80, and 80-100. Each interval included five classes (PN, UL, SIS, CIS, NFW) with a total of 2×10^5 samples (4×10^4 per class). The data were divided into training and testing subsets with a 9:1 split. Model performance was quantified using Accuracy, Precision, Recall, F_1 score, and Macro Average metrics. Additionally, confusion matrices (Fig. 12) and ROC curves (Fig. 11) were plotted to visualise class separation across different SNR regimes. Quantitative metrics for each interval are summarised in Tables 6-10, and the evolution of accuracy, average F_1, and average AUC with increasing SNR is shown in Fig. 10.

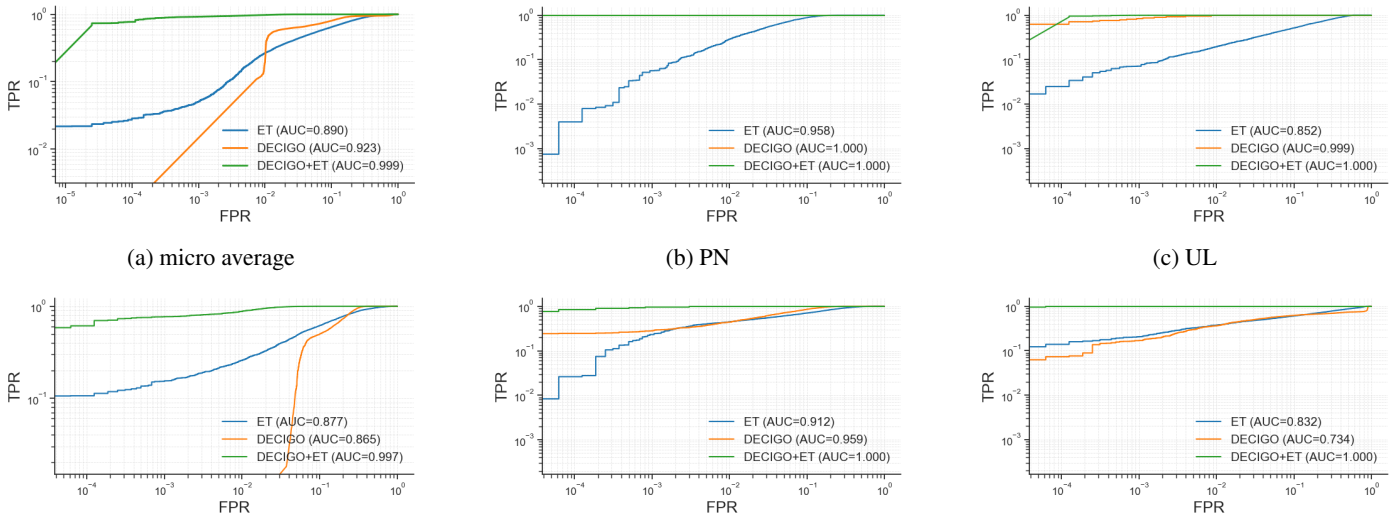

(a) micro average (b) PN (c) UL

(d) SIS (e) CIS (f) NFW

Fig. 8: Comparison of ROC curves across five classification tasks: (a) micro average, (b) PN, (c) UL, (d) SIS, (e) CIS, and (f) NFW.

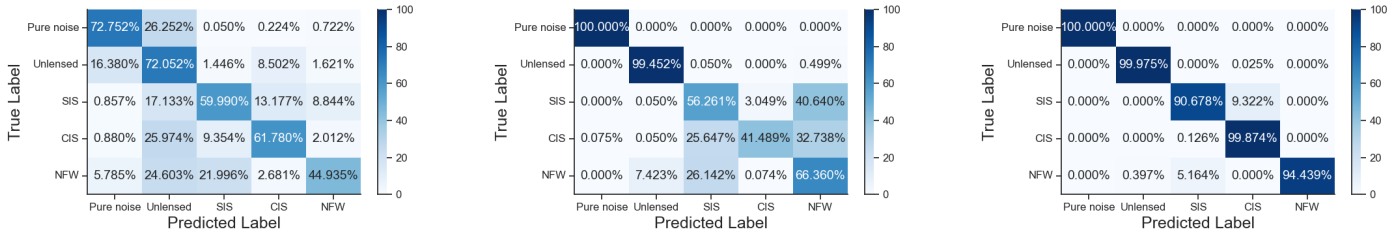

(a) ET (b) DECIGO (c) ET+DECIGO

Fig. 9: Comparison of confusion matrices for three configurations: (a) ET, (b) DECIGO, and (c) joint (ET+DECIGO).

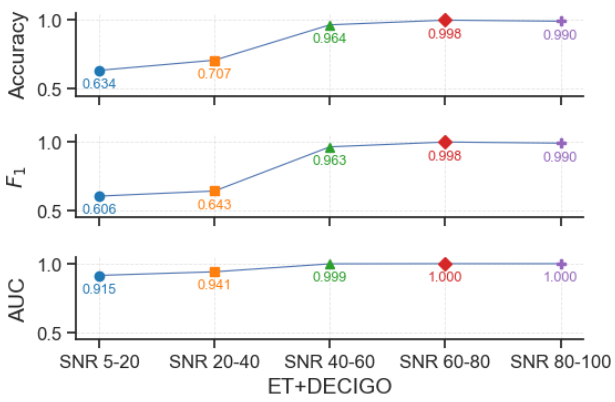

Fig. 10: The classification Accuracy, average F_1, and average AUC for the joint (ET+DECIGO) model across five SNR intervals.

Table 7: Classification metrics of the joint (ET+DECIGO) model in the SNR range 20–40.

Class	Precision	Recall	F_1 score
PN	1.0000	0.9975	0.9987
UL	0.9081	0.9792	0.9423
SIS	0.5473	0.6379	0.5891
CIS	0.8431	0.0109	0.0215
NFW	0.5239	0.8991	0.6620
Macro average	0.7645	0.7049	0.6427
Accuracy		0.7074	

Table 8: Classification metrics of the joint (ET+DECIGO) model in the SNR range 40–60.

Class	Precision	Recall	F_1 score
PN	1.0000	1.0000	1.0000
UL	0.9997	1.0000	0.9999
SIS	0.8472	0.9992	0.9170
CIS	1.0000	0.8196	0.9009
NFW	0.9993	0.9998	0.9995
Macro average	0.9692	0.9637	0.9634
Accuracy		0.9642	

At the lowest SNR interval (5-20), model performance is strongly degraded by noise contamination. The accuracy reaches only 0.6339, and the macro averaged F_1 score is 0.6059 (Table 6). While the "PN" class is perfectly identified (F_1 = 1.000), the "UL" and three lensed classes exhibit substantial confusion. The confusion matrix (Fig. 12a) shows that SIS and CIS suffer the most from mutual misclassification, with correct recognition rates of about 39% and 15%, respectively, and a fraction of samples incorrectly labelled as NFW. This indicates that at low SNR, waveform interference features are heavily masked by noise, hindering the network's ability to extract stable phase dependent structures. The ROC curves (Figs. 11d, 11e, and 11f)

Table 9: Classification metrics of the joint (ET+DECIGO) model in the SNR range 60–80.

Class	Precision	Recall	F_1 score
PN	1.0000	1.0000	1.0000
UL	0.9997	1.0000	0.9999
SIS	1.0000	0.9914	0.9957
CIS	0.9915	1.0000	0.9957
NFW	1.0000	0.9998	0.9999
Macro average	0.9982	0.9982	0.9982
Accuracy		0.9983	

Table 10: Classification metrics of the joint (ET+DECIGO) model in the SNR range 80–100.

Class	Precision	Recall	F_1 score
PN	1.0000	1.0000	1.0000
UL	0.9997	1.0000	0.9999
SIS	0.9989	0.9522	0.9750
CIS	0.9544	1.0000	0.9767
NFW	1.0000	0.9988	0.9994
Macro average	0.9906	0.9902	0.9902
Accuracy		0.9903	

show that the AUC values for the three lensed classes remain in the range 0.84-0.85, suggesting partial robustness to noise but limited discriminative confidence. In this regime, the joint model's advantage is not yet fully realised, being primarily constrained by the low SNR boundary of the input data.

As the SNR increases to moderate levels (20-40 and 40-60), the model performance improves markedly. In the 20-40 range, the accuracy rises to 0.7074 (Table 7), and the macro averaged F_1 score reaches 0.6427. Both SIS and NFW exhibit substantial gains relative to the low SNR regime, with $F_{1,\mathrm{SIS}}$ improving from 0.4431 to 0.5891 and $F_{1,\mathrm{NFW}}$ from 0.5496 to 0.6620. The CIS class, however, remains poorly classified, with $F_1 = 0.0215$.

At SNRs of 40-60, performance increases sharply: accuracy reaches 0.9642 (Table 8), and the macro averaged F_1 rises to 0.9634. The five classes become nearly perfectly separated, with "PN" and "UL" achieving $F_1 = 1.000$. Among the lensed signals, $F_{1,\mathrm{SIS}} = 0.9170$, $F_{1,\mathrm{CIS}} = 0.9009$, and $F_{1,\mathrm{NFW}} = 0.9995$. The confusion matrix (Fig. 12c) exhibits clear diagonal dominance, with residual misclassifications below 20%. The ROC curves (Fig. 11) show AUC values exceeding 0.9 for all classes, with an average AUC near 0.99, confirming the model's capacity to distinguish diffraction and geometric magnification features at moderate SNRs. The accuracy, average F_1, and average AUC in Fig. 10 displays a distinct transition around an SNR of 40, indicating that multiple detector data fusion becomes particularly effective beyond this threshold.

At high SNR (60-100), model performance approaches saturation. In the 60-80 SNR interval, accuracy reaches 0.9983 (Table 9), and the macro averaged F_1 is 0.9982, with both Precision and Recall for all classes nearly unity. The confusion matrix (Fig. 12d) is almost perfectly diagonal, showing only negligible misclassifications.

In the 80-100 SNR range, accuracy slightly decreases to 0.9903 (Table 10), mainly due to minor boundary overlaps among classes, but remains close to ideal. The F_1 scores are $F_{\mathrm{SIS}} = 0.9750$, $F_{1,\mathrm{CIS}} = 0.9767$, and $F_{1,\mathrm{NFW}} = 0.9994$. The ROC curves (Figs. 11a and 11b) show AUC ≈ 1.000, confirming that the model achieves near perfect discrimination at high SNR. The confusion matrix (Fig. 12e) further verifies precise classification across all five classes, with virtually no off diagonal errors.

The overall trend (Fig. 10) reveals a rapid convergence of model performance with increasing SNR—from 63.4% accuracy in the 5-20 range to 99.8% in the 60-80 interval—followed by stability at higher SNRs. These results confirm that the multiple detector configuration substantially enhances the extraction of interference and amplitude features at low to moderate SNRs, while maintaining calibrated probability outputs and precise classification at high SNR. Combining the results in Tables 6-10 and Figs. 11-12, it is evident that the ET+DECIGO model achieves consistently high accuracy and robustness across all SNR regimes, highlighting the crucial role of multiband information fusion in detecting lensed GWs under noise conditions.

7. Conclusion and Outlook

This study proposes a systematic framework for lensed GWs identification under future multiband observations, integrating deep learning with multiband data fusion, and presents comprehensive experiments using simulated data from the ET and DECIGO detectors. The central goal is to develop and preliminarily evaluate an efficient algorithm capable of automatically identifying different lensing classes in complex noise environments, addressing the need for rapid and high precision classification in next generation detectors. The work first outlines the relevant physical mechanisms and then constructs a standardized multiple SNR dataset spanning an SNR range of 5 to 100 and five signal classes. The model employs an improved residual convolutional neural network that directly processes time domain waveforms. Two sets of experiments are conducted to evaluate model performance. The first trains single detector models for ET and DECIGO and a joint detector model for ET plus DECIGO across the full SNR range to evaluate the effect of combining detectors. The second trains the joint model within specific SNR intervals to analyze performance variation with signal strength. Results suggest that the joint model maintains stable accuracy at low SNR and achieves higher accuracy and macro averaged F_1 scores than either single detector model, indicating that multiband feature fusion may benefit weak signal recognition. The study provides a practical framework for multiband lensed GWs identification, demonstrates the capability of deep learning in complex noise environments, and offers a reproducible baseline for future joint observation data analysis.

Future research can further extend and refine this framework in several directions. In data generation, incorporating more diverse lens models, such as ellipsoidal potentials (Hawken & Bridle 2009) and double lens systems (Collett & Bacon 2016; Vegetti et al. 2024), may enhance the adaptability and generalization of the model in complex lensing environments. On the algorithmic side, future studies could investigate network architectures that integrate time and frequency domain representations, or introduce attention mechanisms to better capture long timescale features (Chen et al. 2023; Brauwers & Frasincar 2021). Joint task learning strategies may also enable simultaneous lens classification and parameter estimation, for example, predicting lens mass or impact parameter. The proposed approach can be further evaluated under more realistic observational conditions, including multiple overlapping sources, non stationary noise, and anisotropic detector responses, to examine its robustness and scalability. As third generation ground based detectors (ET) and space detectors (DECIGO, LISA (Amaro-Seoane et al. 2017), Taiji (Ruan et al. 2020), TianQin (Luo et al. 2016)) continue to advance, multiband and multiband observations are expected to

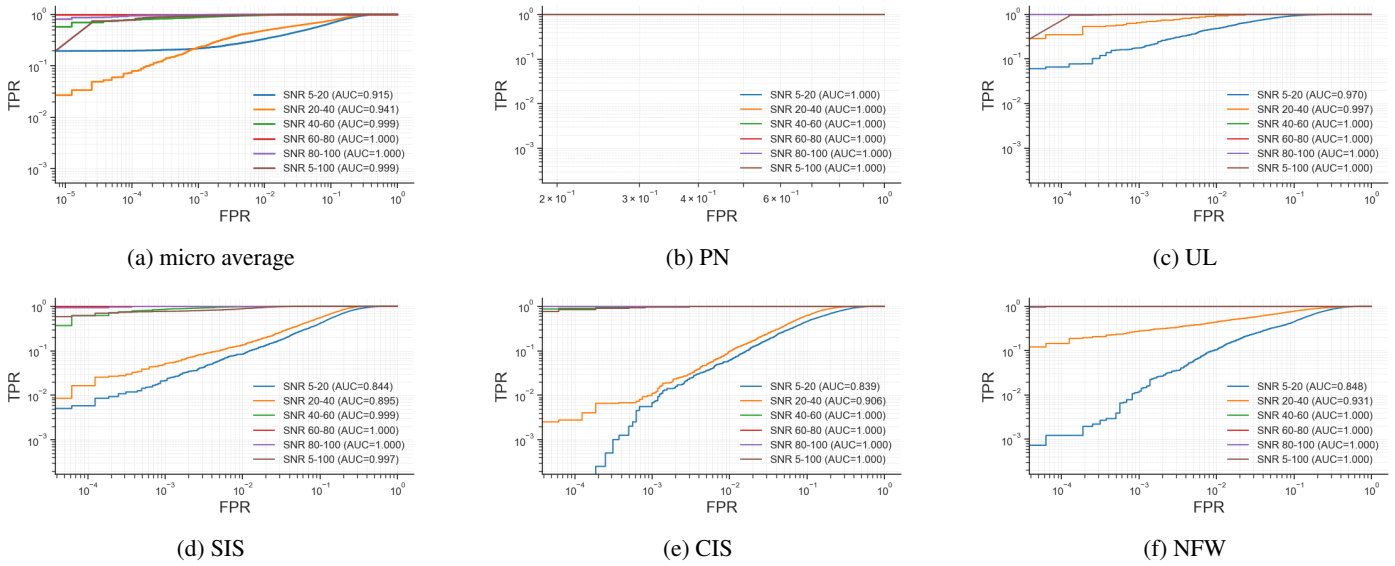

(a) micro average (b) PN (c) UL

(d) SIS (e) CIS (f) NFW

Fig. 11: Comparison of ROC curves for five classification tasks across SNR intervals: (a) micro average, (b) PN, (c) UL, (d) SIS, (e) CIS, and (f) NFW.

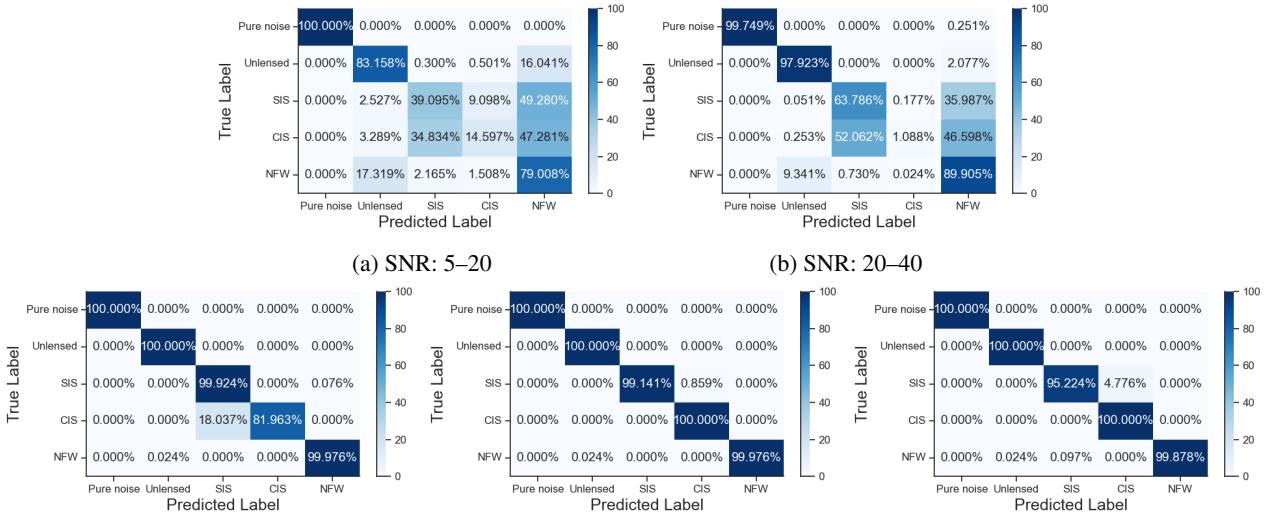

(a) SNR: 5–20 (b) SNR: 20–40

(c) SNR: 40–60 (d) SNR: 60–80 (e) SNR: 80–100

Fig. 12: Confusion matrices of the joint (ET+DECIGO) model across different SNR intervals.

play an increasingly important role in gravitational wave astronomy. Within this context, the present framework offers a useful foundation for rapid identification of lensed GWs, inference of lens parameters, and statistical investigations related to dark matter and cosmology, contributing to the ongoing development of precision gravitational wave astrophysics.

Acknowledgements

This work was supported by the National Key Research and Development Program of China (Grant No. 2021YFC2203004), the Fundamental Research Funds for the Central Universities Project (Grant No. 2024IAIS-ZD009), the National Natural Science Foundation of China (Grant Nos. 12575072 and 12347101), and the Natural Science Foundation of Chongqing (Grant No. CSTB2023NSCQ-MSX0103). This work made use of `TensorFlow` (Abadi et al. 2015), `PyCBC` (Nitz et al. 2024), `GLoW_public` (Villarrubia-Rojo et al. 2025), and other open source Python packages.

References

Abadi, M., Agarwal, A., Barham, P., et al. 2015, TensorFlow, Large-scale machine learning on heterogeneous systems
Abbott, B. P., Abbott, R., Abbott, T., et al. 2020a, The Astrophysical Journal, 892, L3
Abbott, B. P., Abbott, R., Abbott, T., et al. 2017a, The Astrophysical Journal Letters, 848, L13
Abbott, B. P., Abbott, R., Abbott, T. D., et al. 2016a, Physical review letters, 116, 241103
Abbott, B. P., Abbott, R., Abbott, T. D., et al. 2016b, Physical review letters, 116, 061102
Abbott, B. P., Abbott, R., Abbott, T. D., et al. 2017b, Physical review letters, 119, 161101
Abbott, R., Abbott, T., Abraham, S., et al. 2020b, Physical review letters, 125, 101102
Abbott, R., Abbott, T., Abraham, S., et al. 2020c, Physical Review D, 102, 043015

Abbott, R., Abbott, T. D., Abraham, S., et al. 2021, The Astrophysical journal letters, 915, L5
Abe, K. T., Arai, S., Inui, R., et al. 2025, arXiv preprint arXiv:2506.07507
Ade, P. A., Aghanim, N., Arnaud, M., et al. 2016, Astronomy & Astrophysics, 594, A13
Aghanim, N. et al. 2020, Astron. Astrophys, 641, A6
Alam, S., Aubert, M., Avila, S., et al. 2021, Physical Review D, 103, 083533
Amaro-Seoane, P., Audley, H., Babak, S., et al. 2017, arXiv preprint arXiv:1702.00786
Blanchet, L. 2019, Comptes Rendus Physique, 20, 507
Blanchet, L. 2024, Living Reviews in Relativity, 27, 4
Brauwers, G. & Frasincar, F. 2021, IEEE transactions on knowledge and data engineering, 35, 3279
Bulbul, E., Markevitch, M., Foster, A., et al. 2014, The Astrophysical Journal, 789, 13
Chen, Z., Ma, M., Li, T., Wang, H., & Li, C. 2023, Information Fusion, 97, 101819
Cho, G., Porto, R. A., & Yang, Z. 2022, Physical Review D, 106, L101501
Collaboration, L. S., Collaboration, V., et al. 2021, Astrophysical Journal Letters, 915, 1
Collett, T. E. & Bacon, D. J. 2016, Monthly Notices of the Royal Astronomical Society, 456, 2210
Dai, L., Li, S.-S., Zackay, B., Mao, S., & Lu, Y. 2018, Physical Review D, 98, 104029
Dai, L. & Venumadhav, T. 2017, arXiv preprint arXiv:1702.04724
DLT40 Collaboration et al. 2017, Nature, 551, 85
Ehlers, J. & Schneider, P. 2005, in Relativistic Gravity Research With Emphasis on Experiments and Observations: Proceedings of the 81 WE-Heraeus-Seminar Held at the Physikzentrum, Bad Honnef, Germany 2–6 September 1991, Springer, 1–45
Flores, R. A. & Primack, J. R. 1996, The Astrophysical Journal, 457, L5
Goyal, S., Kapadia, S. J., & Ajith, P. 2021, Physical Review D, 104, 124057
Hawken, A. & Bridle, S. 2009, Monthly Notices of the Royal Astronomical Society, 400, 1132
Hild, S., Abernathy, M., Acernese, F. e., et al. 2011, Classical and Quantum gravity, 28, 094013
Hild, S., Chelkowski, S., Freise, A., et al. 2009, Classical and Quantum Gravity, 27, 015003
Janquart, J., Hannuksela, O. A., Haris, K., & Van Den Broeck, C. 2021, Monthly Notices of the Royal Astronomical Society, 506, 5430
Kawamura, S., Ando, M., Seto, N., et al. 2021, Progress of Theoretical and Experimental Physics, 2021, 05A105
Kelly, P. L., Rodney, S., Treu, T., et al. 2023, Science, 380, eabh1322
Kim, K., Lee, J., Yuen, R. S., Hannuksela, O. A., & Li, T. G. 2021, The Astrophysical Journal, 915, 119
Koposov, S., Belokurov, V., Evans, N., et al. 2008, The Astrophysical Journal, 686, 279
Kormann, R., Schneider, P., & Bartelmann, M. 1994, Astronomy and Astrophysics (ISSN 0004-6361), vol. 284, no. 1, p. 285-299, 284, 285
Leung, C., Jow, D., Saha, P., et al. 2025, Space Science Reviews, 221, 1
Li, A. K., Lo, R. K., Sachdev, S., et al. 2023, Physical Review D, 107, 123014
Li, D., Liu, T., Liu, A., et al. 2025, arXiv preprint arXiv:2508.19311
Li, S.-S., Mao, S., Zhao, Y., & Lu, Y. 2018, Monthly Notices of the Royal Astronomical Society, 476, 2220
Liu, A., Liu, T., Li, D., et al. 2025, arXiv preprint arXiv:2509.04538
Luo, J., Chen, L.-S., Duan, H.-Z., et al. 2016, Classical and Quantum Gravity, 33, 035010
Matsunaga, N. & Yamamoto, K. 2006, Journal of Cosmology and Astroparticle Physics, 2006, 023
Mukherjee, S., Wandelt, B. D., & Silk, J. 2020, Physical Review D, 101, 103509
Nakamura, T. T. & Deguchi, S. 1999, Progress of Theoretical Physics Supplement, 133, 137
Navarro, J. F. 1996, in Symposium-international astronomical union, Vol. 171, Cambridge University Press, 255–258
Navarro, J. F., Frenk, C. S., & White, S. D. 1997, The Astrophysical Journal, 490, 493
Nitz, A., Harry, I., Brown, D., et al. 2024, gwastro/pycbc: v2.3.3 release of PyCBC
Pascale, M., Frye, B. L., Pierel, J. D., et al. 2025, The Astrophysical Journal, 979, 13
Perlmutter, S., Aldering, G., Goldhaber, G., et al. 1999, The Astrophysical Journal, 517, 565
Peters, P. C. 1974, Physical Review D, 9, 2207
Poon, J. S., Rinaldi, S., Janquart, J., Narola, H., & Hannuksela, O. A. 2025, Monthly Notices of the Royal Astronomical Society, 536, 2212
Punturo, M., Abernathy, M., Acernese, F., et al. 2010, Classical and Quantum Gravity, 27, 194002
Regimbau, T., Dent, T., Del Pozzo, W., et al. 2012, Physical Review D—Particles, Fields, Gravitation, and Cosmology, 86, 122001
Riess, A. G., Filippenko, A. V., Challis, P., et al. 1998, The astronomical journal, 116, 1009
Ruan, W.-H., Guo, Z.-K., Cai, R.-G., & Zhang, Y.-Z. 2020, International Journal of Modern Physics A, 35, 2050075
Schneider, P. 2005, in Gravitational Lenses: Proceedings of a Conference Held in Hamburg, Germany 9–13 September 1991, Springer, 196–208
Scolnic, D. M., Jones, D., Rest, A., et al. 2018, The Astrophysical Journal, 859, 101
Singh, A. J., Li, I. S., Hannuksela, O. A., Li, T. G., & Kim, K. 2018, arXiv preprint arXiv:1810.07888
Takahashi, R. & Nakamura, T. 2003, The Astrophysical Journal, 595, 1039
Tambalo, G., Zumalacárregui, M., Dai, L., & Cheung, M. H.-Y. 2023, Physical Review D, 108, 043527
Treu, T. 2010, Annual Review of Astronomy and Astrophysics, 48, 87
Tsuji, K., Ishikawa, T., Umemura, K., et al. 2024, Galaxies, 12, 13
Vegetti, S., Birrer, S., Despali, G., et al. 2024, Space Science Reviews, 220, 58
Villarrubia-Rojo, H., Savastano, S., Zumalacárregui, M., et al. 2025, Physical Review D, 111, 103539
Wilde, J., Serjeant, S., Bromley, J. M., et al. 2022, Monthly Notices of the Royal Astronomical Society, 512, 3464
Wu, J., Li, J., Liu, X., & Cao, Z. 2024, Physical Review D, 109, 104014
Yagi, K. & Seto, N. 2011, Physical Review D—Particles, Fields, Gravitation, and Cosmology, 83, 044011